Association between a Failed Prominence Eruption and the Drainage of Mass from Another Prominence

Jianchao Xue [1*], Li Feng [1,2], Hui Li[† 1,2], Ping Zhang [1], Jun Chen [1], Guanglu Shi [1,2], Kaifan Ji [3], Ye Qiu [4], Chuan Li [4,5], Lei Lu [1], Beili Ying [1], Ying Li [1,2], Yu Huang [1], Youping Li [1], Jingwei Li [1], Jie Zhao [1], Dechao Song [1], Shuting Li [1,2], Zhengyuan Tian [1,2], Yingna Su [1,2], Qingmin Zhang [1], Yunyi Ge [1], Jiahui Shan [1,2], Qiao Li [1,2], Gen Li [1,2], Yue Zhou [1,2], Jun Tian [1,2], Xiaofeng Liu [1,2], Zhichen Jing [1,2], Bo Chen [6], Kefei Song [6], Lingping He [6], Shijun Lei [1], Weiqun Gan [1,7]

[1]Key Laboratory of Dark Matter and Space Astronomy, Purple Mountain Observatory, Chinese Academy of Sciences, 10 Yuanhua Road, Nanjing 210023, People's Republic of China

[2]School of Astronomy and Space Science, University of Science and Technology of China, 96 Jinzhai Road, Hefei 230026, People's Republic of China

[3]Yunnan Observatories, Chinese Academy of Sciences, Kunming 650216, People's Republic of China

[4]School of Astronomy and Space Science, Nanjing University, Nanjing 210023, People's Republic of China

[5]Key Laboratory for Modern Astronomy and Astrophysics (Nanjing University), Ministry of Education, Nanjing 210023, People's Republic of China

[6]Changchun Institute of Optics, Fine Mechanics and Physics, Chinese Academy of Sciences, 3888 Dong Nanhu Road, Changchun 130033, People's Republic of China

[7]University of Chinese Academy of Sciences, Nanjing 211135, People's Republic of China

Abstract: Sympathetic eruptions of solar prominences have been studied for decades, however, it is usually difficult to identify their causal links. Here we present two failed prominence eruptions on 26 October 2022 and explore their connections. Using stereoscopic observations, the south prominence (PRO-S) erupts with untwisting motions, flare ribbons occur underneath, and new connections are formed during the eruption. The north prominence (PRO-N) rises up along with PRO-S, and its upper part disappears due to catastrophic mass draining along an elongated structure after PRO-S failed eruption. We suggest that the eruption of PRO-S initiates due to a kink instability, further rises up, and fails to erupt due to reconnection with surrounding fields. The elongated structure connecting PRO-N overlies PRO-S, which causes the rising up of PRO-N along with PRO-S and mass drainage after PRO-S eruption. This study suggests that a prominence may end its life through mass drainage forced by an eruption underneath.

Keywords: Magnetic Reconnection, Observational Signatures; Prominences, Active; Flares, Models

1. Introduction

Solar prominences, or filaments when they are seen on the disk, are dense structures extending into the solar corona (Vial and Engvold, 2015). Cold and dense prominence mass is generally thought to be suspended by the magnetic tension force in magnetic dips (Kippenhahn and Schlüter, 1957; Kuperus and Raadu, 1974). Based on the statistics of Ouyang *et al.* (2017), 11% of filaments have a magnetic flux rope configuration, while others appear as sheared arcades. A magnetic flux rope refers to a set of magnetic field lines winding around a common

---

1

axis more than once (Cheng, Guo, and Ding, 2017). They may suffer from ideal magneto-hydrodynamic (MHD) instabilities, mainly a kink instability (Hood and Priest, 1981) and a torus instability (Kliem and Török, 2006). These instabilities cause eruptions accompanied by large solar flares and coronal mass ejections (CMEs). For a uniformly twisted flux rope, the kink instability sets if the twist number exceeds 1.25 (Hood and Priest, 1981). The torus instability sets if the external poloidal field decreases fast enough, which is evaluated by a decay index. In theory, the critical value of this index for a circular and a straight flux rope is 1.5 and 1, respectively (Démoulin and Aulanier, 2010).

Solar filament eruptions are generally classified into full eruptions, partial eruptions, and failed or confined eruptions (Gilbert, Alexander, and Liu, 2007). The former two types develop into CMEs with significant amounts of high-energy particles and magnetic plasma ejected into the interplanetary space. But for a failed eruption (Ji *et al.*, 2003), neither the prominence mass nor the supporting magnetic structure escapes after an initial acceleration. Causes for the failed eruption of a flux rope can be classified into four types (Chen *et al.*, 2023b; Wang *et al.*, 2023): (1) not reaching the torus instability, where the eruption initiates due to a kink instability (failed kink regime, Török and Kliem, 2005), or the decay index has a saddle-like profile (Guo *et al.*, 2010); (2) failed-torus regime, where a torus-unstable flux rope fails to erupt due to a downward tension force induced by the external toroidal field (Myers *et al.*, 2015; Wang *et al.*, 2023) or a downward Lorentz force by a non-axisymmetry of the flux rope (Zhang *et al.*, 2023b; Zhong, Guo, and Ding, 2021); (3) magnetic reconnection-caused destruction of the flux rope in a breakout-like configuration, where a quadrupolar field is necessary (Chen *et al.*, 2023a,b; DeVore and Antiochos, 2008; Netzel *et al.*, 2012); (4) magnetic reconnection-caused destruction due to the flux rope writhing, the process may happen between the flux rope and the external field, or between the flux rope legs, where the magnetic field configuration could be dipolar (Hassanin and Kliem, 2016; Jiang *et al.*, 2023; Yang *et al.*, 2019; Zhou *et al.*, 2019). In the regimes mentioned above, an eruption initiates in general, though not always, due to MHD instabilities and further accelerates with flare reconnection below the flux rope (Karpen, Antiochos, and DeVore, 2012; Wang *et al.*, 2023). In the breakout configuration, the breakout reconnection initially promotes the eruption through removing the strapping field. However, when the magnetic reconnection between the external field and the flux rope starts, the flux rope is destroyed and upward hoop force decreases, which results in the failure of the eruption (Chen *et al.*, 2023a).

Some eruptions may trigger another eruption, or have a common origin. Solar sympathetic (homologous) eruptions refer to the eruptions that occur at different (the same) sites during a relatively short interval with a certain physical connection (Moon *et al.*, 2003). However for sympathetic eruptions, it is generally difficult to determine whether there is just a chance coincidence. Since solar eruptions in the corona are often dominated by the magnetic field, the causal links between the sympathetic eruptions are generally thought to be of a magnetic nature (Tang *et al.*, 2021). Magnetic reconnection at separatrices, separators, and quasi-separatrix layers is the most common cause for sympathetic eruptions in several works (Liu *et al.*, 2009; Tang *et al.*, 2021; Török *et al.*, 2011; Wang *et al.*, 2018). Magnetic reconnection, along with the expansion of an erupting flux rope (Shen, Liu, and Su, 2012; Yang *et al.*, 2023), mainly plays a role in eroding the overlying field that provides a confining force (Cheng *et al.*, 2013; Li *et al.*, 2017; Liu *et al.*, 2009; Török *et al.*, 2011), and exchanging magnetic flux between flux ropes (Wang *et al.*, 2018). Other authors suggest that perturbations caused by surges, CMEs, and waves can also result in sympathetic eruptions (Dai *et al.*, 2021; Jiang *et al.*, 2011; Wang *et al.*, 2001).

In this work, we report two prominence eruptions on 26 October 2022, where a failed eruption is followed by the catastrophic drainage of mass of another prominence. We analyze the causes of the two eruptions and explore their associations. We introduce the obser-
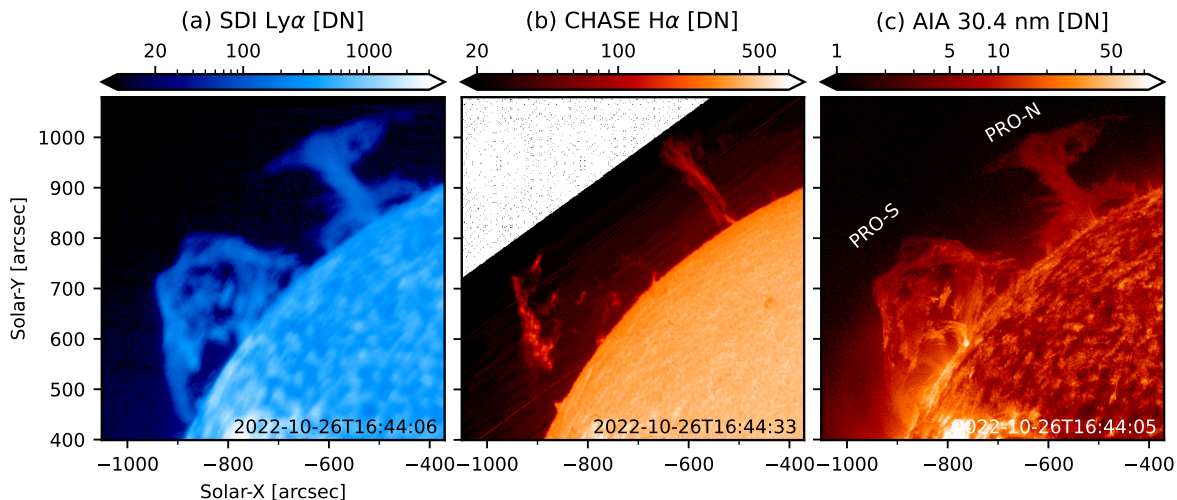
Figure **1**: Prominence images of SDI Lyα, CHASE Hα, and AIA 30.4 nm. An animation of SDI, CHASE Hα line center, and Hα Doppler images from 16:41 to 19:00 UT is attached as supplementary material, see movie_a.mp4. For the animation of AIA 30.4, 17.1, and 19.3 nm observations from 16:26 to 20:30 UT, see movie_b.mp4.

vations in Section 2. Since this is the first light from the Lyman-alpha Solar Telescope (LST, Chen *et al.*, 2019; Feng *et al.*, 2019; Li *et al.*, 2019) onboard the Advanced Space-based Solar Observatory (ASO-S, Gan *et al.*, 2023), emissions in H I Lyα, He II 30.4 nm, and H I Hα lines are compared briefly. In Section 3, the erupting processes of the two prominences are shown. Their eruption causes and association are discussed in Section 4.

2. Observations and Analysis

On 26 October 2022, two solar prominences on the northeastern limb erupted sequentially. Neither flare (by checking GOES soft X-ray light curve) nor associated CME (in the field-of-view of the SOHO/LASCO coronagraph) were found. They were observed by the ASO-S/LST during the commissioning phase. The LST consists of three instruments: a solar disk imager (SDI) in H I Lyα (Lyα for short), a white-light solar telescope (WST) in 360 ± 2 nm waveband, and a solar corona imager (SCI) in both Lyα and white light (700 ± 32 nm). SCI started working in December 2022, hence SCI observations are not available. SDI has a pixel scale of 0.5 arcsec, however, the spatial resolution is worse than that of the Atmospheric Imaging Assembly (AIA, Lemen *et al.*, 2012), i.e., 1.5 arcsec. The SDI cadence is 10 seconds during first light, and data between 15:44 UT and 16:41 UT are lost. SDI level-1 data are dark-field and flat-field corrected. They are aligned to AIA 30.4 nm using cross-correlation and optical flow methods (Cai *et al.*, 2022).

This event was also observed by the Chinese Hα Solar Explorer (CHASE, Li *et al.*, 2022; Qiu *et al.*, 2022) Hα Imaging Spectrograph (HIS). In raster scanning mode, HIS scans the solar disk in 1.2 min with a pixel size of 1.04 arcsec and spectral resoltion of 0.024 Å (0.048 Å in binning mode for this observation). CHASE data are dark-field, slit-image-curvature, and flat-field corrected; wavelength calibration is conducted using two photospheric absorption lines in a quiet region around solar disk center. CHASE maps are co-aligned with the Helioseismic and Magnetic Imager (HMI, Scherrer *et al.*, 2012) continuum images using the scale-invariant feature transform (SIFT, Ji *et al.*, 2017; Lowe, 2004). Figure **1** shows snapshots of the prominence eruptions in SDI Lyα, CHASE Hα, and AIA 30.4 nm. Though SDI has
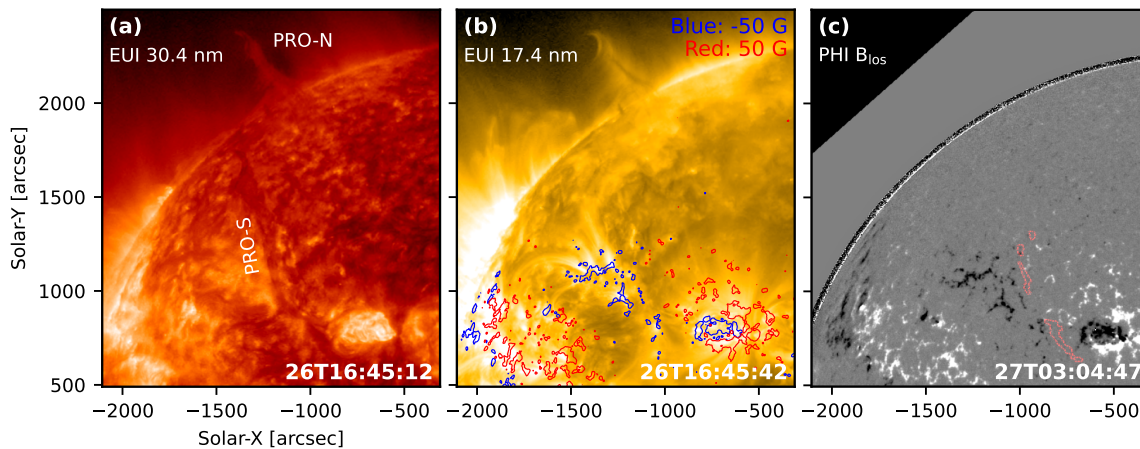
Figure **2**: Maps in Solar Orbiter view. (a)–(b) EUI-FSI 30.4 and 17.4 nm maps at 16:45 UT on 26 October 2022. (c) PHI B_{los} at 3:04 UT on 27 October 2022. The blue and red contours in (b) represent B_{los} of -50 and 50 G, respectively. The contours in (c) mark the PRO-S location, which are extracted from EUI 30.4 nm at 2:00 UT on 26 October 2022. An animation of EUI 30.4 and 17.4 nm observations from 10:05 UT on 26 October to 4:25 UT on 27 October is available as supplementary material, see movie_c.mp4.

a lower spatial resolution than AIA 30.4 nm images, SDI has larger counts, hence a higher signal to noise ratio.

The Lyα lines of both H I at 121.6 nm and He II at 30.4 nm are among the brightest lines of the solar spectrum. On the basis of irradiance and imaging observations, it is found that their intensities have a close relationship (Auchère, 2005; Gordino *et al.*, 2022). For the emission of 121.6 nm and 30.4 nm lines from prominences, resonant scattering of chromspheric radiation is an important contributor (Zhao *et al.*, 2022). Compared with them, the H I Hα line at 656.28 nm is relatively optically thin and mainly contributed from the prominence core (Gouttebroze, Heinzel, and Vial, 1993). This is the main reason why the prominences in Figure **1** look thinner in Hα than those seen in Lyα and 30.4 nm images. Using a non-LTE radiative transfer simulation, Gouttebroze, Heinzel, and Vial (1993) found that the Hα brightness is mainly determined by the prominence emission measure (EM $= \int n_e^2 \mathrm{d}z$ where n_e is the electron density and z is distance along the line-of-sight). Hence the left (south) leg of the south prominence, PRO-S in abbreviation, should have a larger EM than its spine and right leg during its eruption. This brightness distribution suggests that the PRO-S eruption is asymmetric.

With respect to Earth view, the Solar Orbiter (García Marirrodriga *et al.*, 2021) is at the eastern side with an angle of around $46°$. The prominences observed by the Full Sun Imager (FSI) of the Extreme Ultraviolet Imager (EUI, Rochus *et al.*, 2020; SolO/EUI Data Release 6.0 January 2023) are shown in Figure **2**, where the erupting PRO-S is seen as a solar filament, and the north prominence, PRO-N, is still above the solar limb. EUI-FSI 30.4 and 17.4 nm images have a pixel scale of 4.44 arcsec, corresponding to 1.32 Mm pixel^{-1} as the distance of Solar Orbiter from the Sun is $\approx$ 0.41 AU. EUI-FSI has a lower cadence of 10 or 20 minutes than AIA EUV images of 12 seconds. EUI 17.4 nm images are mainly contributed by the emission from Fe X and Fe IX, similar to AIA 17.1 nm channel dominated by Fe IX lines with characteristic emission temperature of 0.63 MK. There is no observation from the EUI High Resolution Imager (HRI). Observations of the Polarimetric and Helioseismic Imager (PHI, Solanki *et al.*, 2020) related to this event started from 27 October 2022 at 3:04 UT. A snapshot of PHI line-of-sight magnetic field (B_{los}) is shown in Figure **2**c, where white (black)
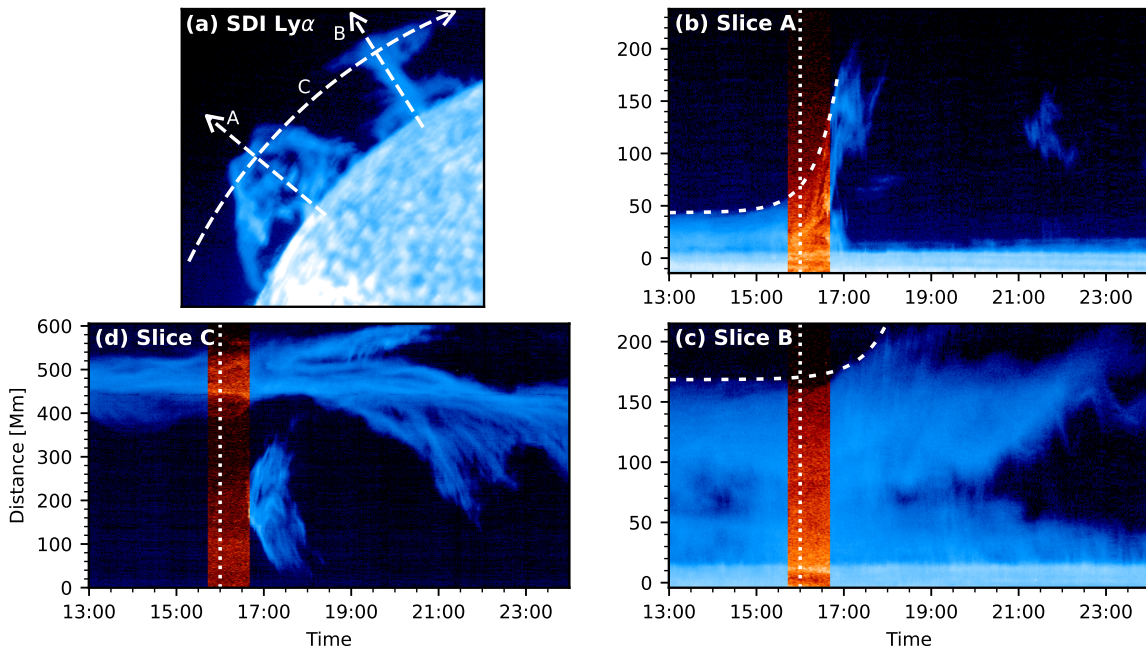
Figure **3**: Time-distance diagrams of prominence eruptions. (a) SDI map with the location of artificial slices indicated, and arrows representing directions of the slices. (b)–(d) Time-distance diagrams along slices A–C, the blue parts are from SDI images and the red parts are AIA 30.4 nm observations.

represents positive (negative) polarities, and the overlaid contours mark the PRO-S location at 2:00 UT on 26 October 2022 extracted from an EUI 30.4 nm image. PHI has a pixel scale of 3.57 arcsec, and the vector magnetogram from PHI is not available for this event. The difference in light travel time between Solar Orbiter and Earth-orbit telescopes is corrected and the time at Earth is used in this article. Figure **2** shows that PRO-S is an intermediate filament and PRO-N is a polar-crown one.

3. Results

3.1. Time-Distance Diagrams of the Erupting Prominences

To trace the dynamical evolution of the prominences, time-distance diagrams are synthesized along three artificial slices (Figure **3**). Among them, slices A and B are perpendicular to the solar limb and almost along the rising trajectories of PRO-S and PRO-N, respectively. Slice C is parallel with the solar limb. Considering that SDI images have a larger signal-to-noise ratio, we mainly used SDI observations and the missing parts are replaced by AIA 30.4 nm images (shown in blue and red respectively in Figures **3**b–d). The height variations of PRO-S and PRO-N, with respect to the solar limb, are fitted using a function composed of a linear part and an exponential part (Cheng *et al.*, 2013, dashed lines in Figure **3**b–c). The rising speeds of PRO-S and PRO-N are calculated to be around 70 and 45 km s^{-1}, respectively, at the end of the fitting. The time 16:00 UT is marked with vertical dotted lines to compare the eruptions of the two prominences.

From Figure **3**b–c, it is seen that PRO-S starts erupting before 16:00 UT and PRO-N rises up following PRO-S. Though no CME is found following their eruptions, PRO-S is fully destroyed but the bottom part of PRO-N survives. In Figure **3**d, the lower (south) structure is PRO-S and the upper (north) one is PRO-N. During the PRO-S eruption, part of PRO-N mass flows northwards in the plane-of-sky (PoS); after PRO-S eruption, PRO-N mass flows
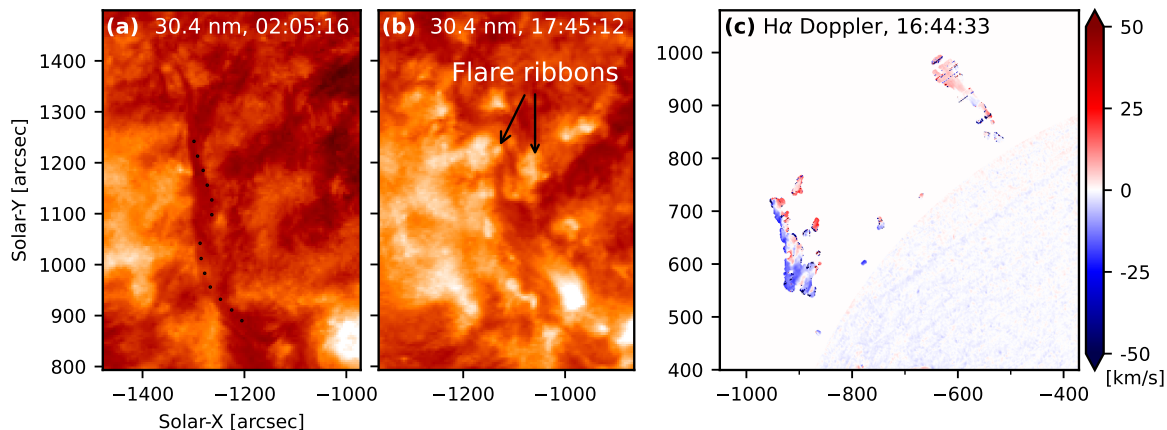
Figure 4: Clues of causes of PRO-S eruption. (a)–(b) EUI 30.4 nm snapshots on 26 October 2022 at 2:05 and 17:45 UT, respectively. (c) Hα Doppler map on 26 October 2022 at 16:44 UT.
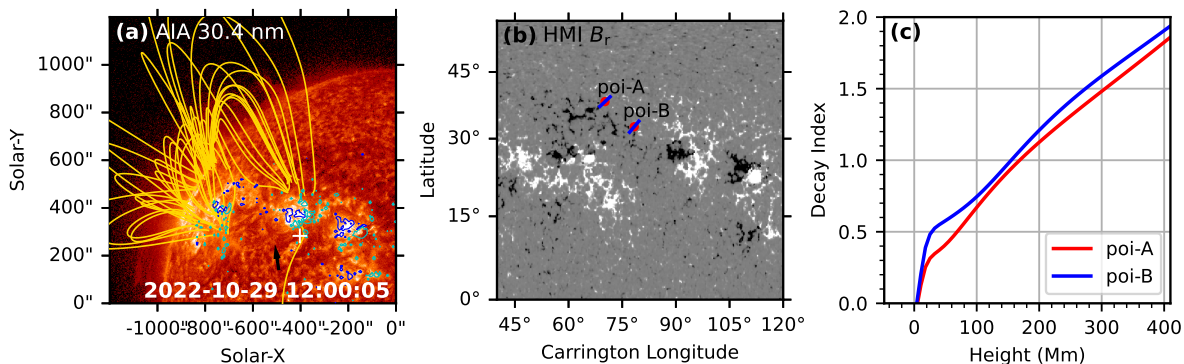

Figure 5: Potential field configuration and decay index. (a) AIA 30.4 nm snapshots on 29 October 2022 at 12:00 UT and extrapolated magnetic field configuration, where only closed field is plotted as golden lines. Blue and cyan contours represent B_{los} of -100 and 100 G, respectively. (b) B_{r} Carrington map from HMI observations. (c) Decay index along height.

oppositely. The motion of PRO-N is likely to be associated with the PRO-S eruption.

3.2. Phenomena Related to PRO-S Eruption

As mentioned in Section 1, the initiation and failing of an eruption can be related to a kink instability, a torus instability, and reconnection below or/and around the flux rope, in addition to external triggers. We explore the eruption of PRO-S in relation with these mechanisms.

Figure 4a–b shows snapshots of EUI 30.4 nm maps of PRO-S. Around 14 hours before the PRO-S eruption (Figure 4a), a flux rope with a twist number of nearly 2 is seen (delineated with dotted curves), and the helicity is negative. Its southern leg roots in the periphery of an active region (AR), and the northern leg finishes in bifurcated ends. During the PRO-S eruption (Figure 4b), flare ribbons are seen underneath. Figure 4c shows a Doppler map from CHASE Hα observations during the PRO-S eruption. A single Gaussian fitting is used to derive the Doppler speeds for simplification (Xue *et al.*, 2021), hence the derived speeds should be treated as an averaged result, or represent the motions of the main component if there are multi-peaks in one Hα profile. Relative to the PRO-S leg axis, the left part is mainly blue-shifted and the right part is red-shifted with velocities within around $\pm 17\,\mathrm{km\,s^{-1}}$. Compared with the negative helicity shown in Figure 4a and assuming that the footpoint is tied,
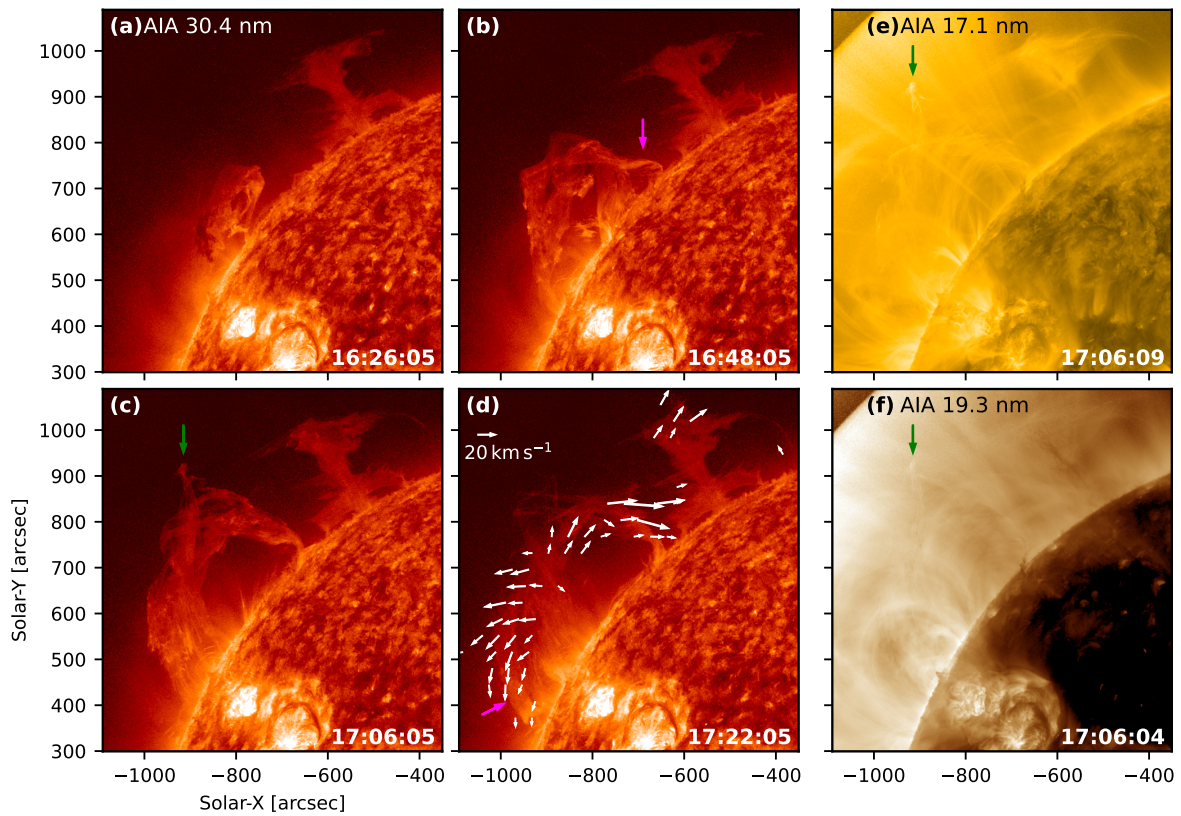
Figure **6**: Process of the PRO-S failed eruption. (a)–(d) AIA 30.4 nm images. White arrows in (d) represent flow in the plane-of-sky. (e) AIA 17.1 nm image. (f) AIA 19.3 nm image. Observation times are marked at lower-right corner in each panel.

the Doppler map in Figure **4**c indicates an untwisting motion.

The threshold of the torus instability is usually given by a critical decay index. The decay index n is defined by

$$n = -\frac{\mathrm{dln}B_{\mathrm{ep}}(R)}{\mathrm{dln}R} , \tag{1}$$

where R denotes the distance to the center of an approximately toroidal flux rope, and B_{ep} denotes the external poloidal field (Chen *et al.*, 2023a). For simplification, we use height to replace R and B_{ep} is assumed to be nearly perpendicular to the polarity inversion line (PIL) based on a potential field approach. Through comparing B_{los} of PHI and HMI, the magnetic field around PRO-S does not vary significantly in the following days. Hence the synoptic Carrington magnetogram of the normal component (B_{r}) from HMI is used to compute the potential field with the *pfsspy* package (Stansby, Yeates, and Badman, 2020). The extrapolated potential field configuration is shown in Figure **5**a over an AIA 30.4 nm map, where only closed field lines are plotted. The blue and cyan contours mark HMI B_{los} of -100 and +100 G, respectively. Though PRO-S erupts on 26 October, the filament channel is clearly seen (pointed by a black arrow, no corresponding filament is seen in the Hα image), which is enveloped by a series of loops. The south footpoint of PRO-S lies on a positive polarity, it can be seen from the overlaid B_{los} contours, and could also be derived from the fact that a negative helicity structure locates along a dextral channel (Martin, Bilimoria, and Tracadas, 1994). The decay index is calculated at two points around the middle point of the projected PRO-S axis along the PIL, marked as poi-A and poi-B in Figure **5**b, and its changes with height are shown in Figure **5**c. From Figure **3**b, the axis of PRO-S reaches a height of around 185 Mm before its disappearance, which should be the lower limit considering the projection effect. The decay index at 185 Mm is ≈ 1, reaching the critical value of the torus instability for a straight current channel, but smaller than 1.5 for a circular shape (Démoulin and Aulanier, 2010). Considering the errors of measurements in this work and the limitations in models, we cannot say whether PRO-S keeps torus stable during the rising process.

Signatures of magnetic reconnection between PRO-S and the ambient coronal loops are explored in Figure **6**, which mainly shows sequential images of PRO-S failed eruption in AIA 30.4 nm. The first signature is the appearance of the new legs formed during the eruption. The two new legs are marked with magenta arrows in Figure **6**b and d. They are filled with PRO-S dropping mass. The second signature is that the rising PRO-S is not regular and a "peak" is marked (green arrow) in Figure **6**c, which is also bright in AIA 17.1 and 19.3 nm images, suggesting that the plasma is heated to coronal temperature. However, because the emission of the PRO-S eruption is relatively weak and no X-ray flare is detected by the GOES, there is no significant brightening around PRO-S. A brightening in X-rays and EUV is usually used as an indication of magnetic reconnection (Chen *et al.*, 2023b; Hassanin and Kliem, 2016; Ji *et al.*, 2003; Netzel *et al.*, 2012). In Figure **6**d, the optical flows (marked with white arrows, calculated using two 30.4 nm images with an interval of 2 minutes) suggest that the PRO-S mass is mainly dropping along the legs and the rising almost stops.

3.3. Phenomena related to PRO-N eruption

The end of PRO-N is in the form of mass drainage after PRO-S failed eruption. Figure **7** shows the draining process in EUI 30.4 and 17.4 nm. Among the panels, the white arrows in panels a, b, e, and f point to the erupting PRO-S; the green arrows point to a cluster of mass that rises faster than PRO-N main body, and stops around the horn-like structure of PRO-N; and the magenta arrows point the mass draining along the horn. Horn-like structures refer to curved extensions that protrude from the top of quiescent prominences into the cavities (Su *et al.*, 2015). In our case, the horn is clearly seen in 17.4 nm images, and the curvature gets
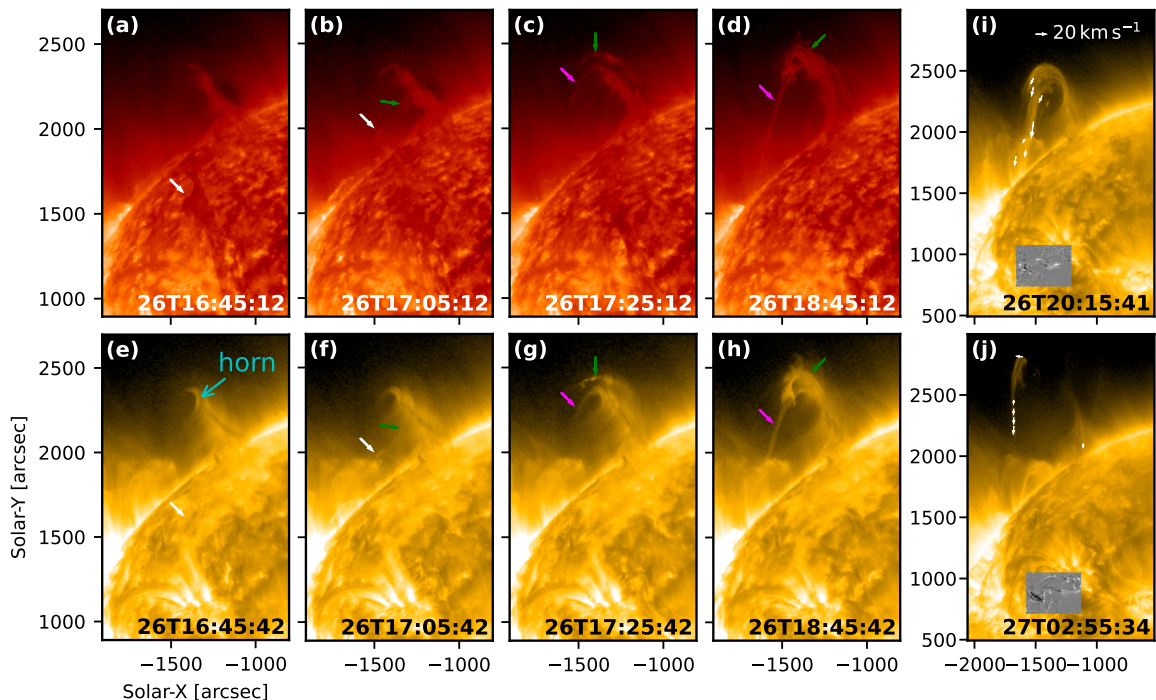
Figure **7**: Time sequence images of EUI 30.4 nm (a-d) and 17.4 nm (e-j) showing PRO-N mass drainage. In (i)–(j), the white arrows represent flows, and the grey insets are difference images.

smaller during the PRO-S rising. After PRO-S failed eruption, the flow along the horn gets significant. Figure **7**i–j shows violent drainage of PRO-N mass along the horn (white arrows mark the optical flow) and the brightening on the disk (difference image of the inset). Due to the projection effect, we cannot identify the other end of the flux tube that connects the PRO-N horn. However, the brightening on the disk has a good temporal correlation with the violent mass drainage (see movie_c.mp4). Hence, we suspect that the PRO-N horn extends southwards and overlies the filament channel where PRO-S is located in before the eruption.

4. Discussion and Conclusion

Through the time-distance diagrams, we have seen that the motion of PRO-N is closely related to PRO-S eruption: PRO-N rises up along with PRO-S, and PRO-N mass moves northwards during PRO-S expansion and moves back after PRO-S failed eruption.

Then we study the causes of PRO-S failed eruption, and mainly explored the evidence of whether kink instability, torus instability, flare reconnection, and reconnection with ambient magnetic field play roles. PRO-S has a twist number of nearly 2 and shows an untwisting motion during the eruption (Figure **4**). Therefore, we suggest that a kink instability happens. A trigger is generally necessary to excite the kink instability, and the trigger resulting in loss of equilibrium could be an oscillation and mass drainage (Bi *et al.*, 2014; Fan, 2020), magnetic reconnection in the rope system (Zhang *et al.*, 2023a) including the one happening in the breakout model (Kumar *et al.*, 2023). The decay index is calculated using an HMI Carrington magnetogram and is found to be around 1 at the height of PRO-S, just reaching the lower limit for the torus instability (1 to 1.5). Hence it is possible that the external field, no matter poloidal or toroidal field once PRO-S rotates, plays a role in confining the eruption. There are some shortcomings if a potential field model is used as an approximation of the real external field. In addition to the problems mentioned in Zhang *et al.* (2023b), the ambient

9

magnetic field may be disturbed by frequent activity. Before the event we study, a faint but large filament eruption occurs around 1:00 UT on 26 October 2022 (see movie_c.mp4). Flare reconnection under a flux rope is thought to be the main cause of explosive CME acceleration (Karpen, Antiochos, and DeVore, 2012). We observe flare ribbons but no post-eruption loops, which suggests that the flare reconnection happens but is very weak during PRO-S eruption. The reconnection between PRO-S and the ambient field is also explored, and new legs filled with dropping prominence mass probably support the occurrence of magnetic reconnection. However, due to the low emission of the eruption (no GOES X-ray flare), the reconnection location cannot be identified from X-ray or EUV radiation. A difference of PRO-S from the generally reported confined eruptions (Chen *et al.*, 2023b) is that no clear deceleration is detected before the disappearance of PRO-S along the rising trajectory (Figure **3**b). We suggest that PRO-S is destroyed by the magnetic reconnection between PRO-S and the overlying field before an obvious deceleration. Considering the observed untwisting motion and expected writhing motion (to keep the conservation of magnetic helicity), it is speculated that the magnetic reconnection happens (see the fourth regime for failed eruptions in Section 1).

A horn-like structure is at the top of PRO-N, along which PRO-N mass drains southwards. Brightening occurs on some regions on the solar disk, and these regions may connect with PRO-N horn through flux tubes. Prominence horn structures are generally thought to be flux ropes or hyperbolic flux tubes holding prominences (Fan, 2012; Su *et al.*, 2015). From the EUI 30.4 nm image in Figure **2**a, RPO-S has an orientation southwest to northeast. We suspect the flux tube connecting PRO-N horn is over PRO-S, which could explain both the rising up of PRO-N along with PRO-S, and mass drainage after PRO-S failed eruption due to evacuation under the flux tube. Once the mass flow starts, it leads to a catastrophic mass drainage of PRO-N because of a siphon effect. Plasma gravity plays an important role in stabilizing a prominence and continuous mass drainage may initiate an eruption (Fan, 2020; Wang *et al.*, 2023). From Figure **7**i–j, PRO-N rises during the violent mass drainage but does not erupt.

The relation between PRO-S and PRO-N is different from the flux rope systems of double-decker above the same PIL (Liu *et al.*, 2012) or side-by-side over different PILs. Due to the limitation of observations, we cannot identify exactly the location of the flux tube that connects with PRO-N horn. Horn structures, not rare for quiescent prominences (Wang *et al.*, 2016), are a part of long flux tubes, including both flux ropes and sheared arcades. Prominence and flux tubes that connect with the horns compose the large scale prominence-cavity systems. They suffer frequent disturbance because of activity underneath including jet and filament eruptions (Chen *et al.*, 2021). From EUI observations, PRO-S is likely to locate below the flux tube that holds PRO-N.

In summary, the sympathetic eruptions in this work could be divided into three stages:

1. PRO-S rises due to a helical kink instability (PRO-S is twisted in EUI 30.4 nm image and an untwisting motion is observed in the Hα Doppler map). Magnetic reconnection occurs under PRO-S (flare ribbons) and provides a positive feedback to the eruption. Because the flux tube that holds PRO-N is over PRO-S, PRO-N also rises up and is pushed away from PRO-S due to the expansion of the latter (time-distance diagrams in Figure **3**).

2. PRO-S reconnects with the overlying magnetic field (new legs appear in Figure **6**), and the upward hoop force decreases along with the decay of the poloidal field of PRO-S. It is possible that the external magnetic field plays a role in confining the eruption.

3. PRO-N mass flow along the horn starts due to the evacuation after PRO-S failed eruption, which leads to the catastrophic mass drainage due to siphon effect (Figure **7**). In the end only the bottom part remains.

Mass draining is a usual form in which prominences end their life, and this work suggests that catastrophic mass draining may result from a filament eruption underneath.

Acknowledgements

References

Auchère, F.: 2005, Effect of the H I Lyα Chromospheric Flux Anisotropy on the Total Intensity of the Resonantly Scattered Coronal Radiation. *Astrophys. J.* **622**(1), 737. DOI. ADS.

Bi, Y., Jiang, Y., Yang, J., Hong, J., Li, H., Yang, D., Yang, B.: 2014, Solar Filament Material Oscillations and Drainage before Eruption. *Astrophys. J.* **790**(2), 100. DOI. ADS.

Cai, Y.-F., Yang, X., Xiang, Y.-Y., Yan, X.-L., Jin, Z.-Y., Liu, H., Ji, K.-F.: 2022, The Co-alignment of Winged Hα Data Observed by the New Vacuum Solar Telescope. *Res. Astron. Astrophys.* **22**(6), 065010. DOI. ADS.

Chen, B., Li, H., Song, K.-F., Guo, Q.-F., Zhang, P.-J., He, L.-P., *et al.*: 2019, The Lyman-alpha Solar Telescope (LST) for the ASO-S mission - II. design of LST. *Res. Astron. Astrophys.* **19**(11), 159. DOI. ADS.

Chen, C., Su, Y., Xue, J., Gan, W., Huang, Y.: 2021, Solar Prominence Bubble and Plumes Caused By an Eruptive Magnetic Flux Rope. *Astrophys. J. Lett.* **923**(1), L10. DOI. ADS.

Chen, J., Cheng, X., Kliem, B., Ding, M.: 2023a, A Model for Confined Solar Eruptions Including External Reconnection. *Astrophys. J. Lett.* **951**(2), L35. DOI. ADS.

Chen, Y., Cheng, X., Chen, J., Dai, Y., Ding, M.: 2023b, Observations of a Failed Solar Filament Eruption Involving External Reconnection. *Astrophys. J.* **959**(2), 67. DOI. ADS.

Cheng, X., Guo, Y., Ding, M.: 2017, Origin and Structures of Solar Eruptions I: Magnetic Flux Rope. *Science China Earth Sciences* **60**, 1383. DOI. ADS.

Cheng, X., Zhang, J., Ding, M.D., Olmedo, O., Sun, X.D., Guo, Y., Liu, Y.: 2013, Investigating Two Successive Flux Rope Eruptions in a Solar Active Region. *Astrophys. J. Lett.* **769**(2), L25. DOI. ADS.

Dai, J., Zhang, Q., Zhang, Y., Xu, Z., Su, Y., Ji, H.: 2021, Oscillations and Mass Draining that Lead to a Sympathetic Eruption of a Quiescent Filament. *Astrophys. J.* **923**(1), 74. DOI. ADS.

Démoulin, P., Aulanier, G.: 2010, Criteria for Flux Rope Eruption: Non-equilibrium Versus Torus Instability. *Astrophys. J.* **718**(2), 1388. DOI. ADS.

DeVore, C.R., Antiochos, S.K.: 2008, Homologous Confined Filament Eruptions via Magnetic Breakout. *Astrophys. J.* **680**(1), 740. DOI. ADS.

Fan, Y.: 2012, Thermal Signatures of Tether-cutting Reconnections in Pre-eruption Coronal Flux Ropes: Hot Central Voids in Coronal Cavities. *Astrophys. J.* **758**(1), 60. DOI. ADS.

Fan, Y.: 2020, Simulations of Prominence Eruption Preceded by Large-amplitude Longitudinal Oscillations and Draining. *Astrophys. J.* **898**(1), 34. DOI. ADS.

Feng, L., Li, H., Chen, B., Li, Y., Susino, R., Huang, Y., *et al.*: 2019, The Lyman-alpha Solar Telescope (LST) for the ASO-S mission - III. data and potential diagnostics. *Res. Astron. Astrophys.* **19**(11), 162. DOI. ADS.

Gan, W., Zhu, C., Deng, Y., Zhang, Z., Chen, B., Huang, Y., *et al.*: 2023, The Advanced Space-Based Solar Observatory (ASO-S). *Solar Phys.* **298**(5), 68. DOI. ADS.

García Marirrodriga, C., Pacros, A., Strandmoe, S., Arcioni, M., Arts, A., Ashcroft, C., *et al.*: 2021, Solar Orbiter: Mission and spacecraft design. *Astron. Astrophys.* **646**, A121. DOI. ADS.

Gilbert, H.R., Alexander, D., Liu, R.: 2007, Filament Kinking and Its Implications for Eruption and Re-formation. *Solar Phys.* **245**(2), 287. DOI. ADS.

Gordino, M., Auchère, F., Vial, J.-C., Bocchialini, K., Hassler, D.M., Bando, T., *et al.*: 2022, Empirical relations between the intensities of Lyman lines of H and He$^+$. *Astron. Astrophys.* **657**, A86. DOI. ADS.

Gouttebroze, P., Heinzel, P., Vial, J.C.: 1993, The hydrogen spectrum of model prominences. *Astron. Astrophys. Suppl.* **99**, 513. ADS.

Guo, Y., Ding, M.D., Schmieder, B., Li, H., Török, T., Wiegelmann, T.: 2010, Driving Mechanism and Onset Condition of a Confined Eruption. *Astrophys. J. Lett.* **725**(1), L38. DOI. ADS.

Hassanin, A., Kliem, B.: 2016, Helical Kink Instability in a Confined Solar Eruption. *Astrophys. J.* **832**(2), 106. DOI. ADS.

Hood, A.W., Priest, E.R.: 1981, Critical conditions for magnetic instabilities in force-free coronal loops. *Geophy. Astrophys. Fluid Dyn.* **17**(1), 297. DOI. ADS.

Ji, H., Wang, H., Schmahl, E.J., Moon, Y.-J., Jiang, Y.: 2003, Observations of the Failed Eruption of a Filament. *Astrophys. J. Lett.* **595**(2), L135. DOI. ADS.

Ji, K., Liu, H., Jin, Z., Shang, Z., Qiang, Z.: 2017, An automatic approach of mapping the solar high-resolution image to Helioprojective-Cartesian coordinates system. *ChSBu* **64**, 1738. DOI. https://doi.org/10.1360/N972019-00092.

Jiang, C., Duan, A., Zou, P., Zhou, Z., Bian, X., Feng, X., *et al.*: 2023, A model of failed solar eruption initiated and destructed by magnetic reconnection. *Mon. Not. Roy. Astron. Soc.* **525**(4), 5857. DOI. ADS.

Jiang, Y., Yang, J., Hong, J., Bi, Y., Zheng, R.: 2011, Sympathetic Filament Eruptions Connected by Coronal Dimmings. *Astrophys. J.* **738**(2), 179. DOI. ADS.

Karpen, J.T., Antiochos, S.K., DeVore, C.R.: 2012, The Mechanisms for the Onset and Explosive Eruption of Coronal Mass Ejections and Eruptive Flares. *Astrophys. J.* **760**(1), 81. DOI. ADS.

Kippenhahn, R., Schlüter, A.: 1957, Eine Theorie der solaren Filamente. Mit 7 Textabbildungen. *Z. für Astrophys.* **43**, 36. ADS.

Kliem, B., Török, T.: 2006, Torus Instability. *Phys. Rev. Lett.* **96**(25), 255002. DOI. ADS.

Kumar, P., Karpen, J.T., Antiochos, S.K., DeVore, C.R., Wyper, P.F., Cho, K.-S.: 2023, Plasmoids, Flows, and Jets during Magnetic Reconnection in a Failed Solar Eruption. *Astrophys. J.* **943**(2), 156. DOI. ADS.

Kuperus, M., Raadu, M.A.: 1974, The Support of Prominences Formed in Neutral Sheets. *Astron. Astrophys.* **31**, 189. ADS.

Lemen, J.R., Title, A.M., Akin, D.J., Boerner, P.F., Chou, C., Drake, J.F., *et al.*: 2012, The Atmospheric Imaging Assembly (AIA) on the Solar Dynamics Observatory (SDO). *Solar Phys.* **275**(1-2), 17. DOI. ADS.

Li, C., Fang, C., Li, Z., Ding, M., Chen, P., Qiu, Y., *et al.*: 2022, The Chinese Hα Solar Explorer (CHASE) mission: An overview. *Sci. China Phys. Mech. Astron.* **65**(8), 289602. DOI. ADS.

Li, H., Chen, B., Feng, L., Li, Y., Huang, Y., *et al.*: 2019, The Lyman-alpha Solar Telescope (LST) for the ASO-S mission — I. Scientific objectives and overview. *Res. Astron. Astrophys.* **19**(11), 158. DOI. ADS.

Li, S., Su, Y., Zhou, T., van Ballegooijen, A., Sun, X., Ji, H.: 2017, High-resolution Observations of Sympathetic Filament Eruptions by NVST. *Astrophys. J.* **844**(1), 70. DOI. ADS.

Liu, C., Lee, J., Karlický, M., Prasad Choudhary, D., Deng, N., Wang, H.: 2009, Successive Solar Flares and Coronal Mass Ejections on 2005 September 13 from NOAA AR 10808. *Astrophys. J.* **703**(1), 757. DOI. ADS.

Liu, R., Kliem, B., Török, T., Liu, C., Titov, V.S., Lionello, R., Linker, J.A., Wang, H.: 2012, Slow Rise and Partial Eruption of a Double-decker Filament. I. Observations and Interpretation. *Astrophys. J.* **756**(1), 59. DOI. ADS.

Lowe, D.G.: 2004, Distinctive Image Features from Scale-Invariant Keypoints. *Int. J. Comput. Vis.* **60**(91). DOI. https://doi.org/10.1023/B:VISI.0000029664.99615.94.

Martin, S.F., Bilimoria, R., Tracadas, P.W.: 1994, Magnetic field configurations basic to filament channels and filaments. In: Rutten, R.J., Schrijver, C.J. (eds.) *Solar Surface Magnetism*, *NATO Advanced Study Institute (ASI) Series C* **433**, 303. ADS.

Moon, Y.-J., Choe, G.S., Wang, H., Park, Y.D.: 2003, Sympathetic Coronal Mass Ejections. *Astrophys. J.* **588**(2), 1176. DOI. ADS.

Myers, C.E., Yamada, M., Ji, H., Yoo, J., Fox, W., Jara-Almonte, J., Savcheva, A., Deluca, E.E.: 2015, A dynamic magnetic tension force as the cause of failed solar eruptions. *Nature* **528**(7583), 526. DOI. ADS.

Netzel, A., Mrozek, T., Kołomański, S., Gburek, S.: 2012, Extreme-ultraviolet and hard X-ray signatures of electron acceleration during the failed eruption of a filament. *Astron. Astrophys.* **548**, A89. DOI. ADS.

Ouyang, Y., Zhou, Y.H., Chen, P.F., Fang, C.: 2017, Chirality and Magnetic Configurations of Solar Filaments. *Astrophys. J.* **835**(1), 94. DOI. ADS.

Qiu, Y., Rao, S., Li, C., Fang, C., Ding, M., Li, Z., *et al.*: 2022, Calibration procedures for the CHASE/HIS science data. *Sci. China Phys. Mech. Astron.* **65**(8), 289603. DOI. ADS.

Rochus, P., Auchère, F., Berghmans, D., Harra, L., Schmutz, W., Schühle, U., *et al.*: 2020, The Solar Orbiter EUI instrument: The Extreme Ultraviolet Imager. *Astron. Astrophys.* **642**, A8. DOI. ADS.

Scherrer, P.H., Schou, J., Bush, R.I., Kosovichev, A.G., Bogart, R.S., Hoeksema, J.T., Liu, Y., Duvall, T.L., Zhao, J., Title, A.M., Schrijver, C.J., Tarbell, T.D., Tomczyk, S.: 2012, The Helioseismic and Magnetic Imager (HMI) Investigation for the Solar Dynamics Observatory (SDO). *Solar Phys.* **275**(1-2), 207. DOI. ADS.

Shen, Y., Liu, Y., Su, J.: 2012, Sympathetic Partial and Full Filament Eruptions Observed in One Solar Breakout Event. *Astrophys. J.* **750**(1), 12. DOI. ADS.

Solanki, S.K., del Toro Iniesta, J.C., Woch, J., Gandorfer, A., Hirzberger, J., Alvarez-Herrero, A., *et al.*: 2020, The Polarimetric and Helioseismic Imager on Solar Orbiter. *Astron. Astrophys.* **642**, A11. DOI. ADS.

SolO/EUI Data Release 6.0 January 2023 DOI.

Stansby, D., Yeates, A., Badman, S.: 2020, pfsspy: A Python package for potential field source surface modelling. *J. Open Sour. Soft.* **5**(54), 2732. DOI. ADS.

Su, Y., van Ballegooijen, A., McCauley, P., Ji, H., Reeves, K.K., DeLuca, E.E.: 2015, Magnetic Structure and Dynamics of the Erupting Solar Polar Crown Prominence on 2012 March 12. *Astrophys. J.* **807**(2), 144. DOI. ADS.

Tang, Z., Shen, Y., Zhou, X., Duan, Y., Zhou, C., Tan, S., Elmhamdi, A.: 2021, Sympathetic Standard and Blowout Coronal Jets Observed in a Polar Coronal Hole. *Astrophys. J. Lett.* **912**(1), L15. DOI. ADS.

Török, T., Kliem, B.: 2005, Confined and Ejective Eruptions of Kink-unstable Flux Ropes. *Astrophys. J. Lett.* **630**(1), L97. DOI. ADS.

Török, T., Panasenco, O., Titov, V.S., Mikić, Z., Reeves, K.K., Velli, M., Linker, J.A., De Toma, G.: 2011, A Model for Magnetically Coupled Sympathetic Eruptions. *Astrophys. J. Lett.* **739**(2), L63. DOI. ADS.

Vial, J.-C., Engvold, O.: 2015, *Solar Prominences*, *Astrophys. Space Sci. Lib.* **415**. DOI. ADS.

Wang, B., Chen, Y., Fu, J., Li, B., Li, X., Liu, W.: 2016, Dynamics of a Prominence-horn Structure during Its Evaporation in the Solar Corona. *Astrophys. J. Lett.* **827**(2), L33. DOI. ADS.

Wang, C., Chen, F., Ding, M., Lu, Z.: 2023, Radiative Magnetohydrodynamic Simulation of the Confined Eruption of a Magnetic Flux Rope: Unveiling the Driving and Constraining Forces. *Astrophys. J.* **956**(2), 106. DOI. ADS.

Wang, D., Liu, R., Wang, Y., Gou, T., Zhang, Q., Zhou, Z., Zhang, M.: 2018, Unraveling the Links among Sympathetic Eruptions. *Astrophys. J.* **869**(2), 177. DOI. ADS.

Wang, H., Chae, J., Yurchyshyn, V., Yang, G., Steinegger, M., Goode, P.: 2001, Inter-Active Region Connection of Sympathetic Flaring on 2000 February 17. *Astrophys. J.* **559**(2), 1171. DOI. ADS.

Xue, J.-C., Vial, J.-C., Su, Y., Li, H., Xu, Z., Su, Y.-N., Zhou, T.-H., Li, Z.-T.: 2021, High-resolution observations of prominence plume formation with the new vacuum solar telescope. *Res. Astron. Astrophys.* **21**(9), 222. DOI. ADS.

Yang, L., Yan, X., Xue, Z., Wang, J., Yang, L., Li, Q., *et al.*: 2023, Sympathetic Partial Filament Eruptions Caused by the Interaction between Two Nearby Filaments. *Astrophys. J.* **943**(1), 62. DOI. ADS.

Yang, S., Zhang, J., Song, Q., Bi, Y., Li, T.: 2019, Two-step Evolution of a Rising Flux Rope Resulting in a Confined Solar Flare. *Astrophys. J.* **878**(1), 38. DOI. ADS.

Zhang, Q., Cheng, X., Liu, R., Song, A., Li, X., Wang, Y.: 2023a, Influence of magnetic reconnection on the eruptive catastrophes of coronal magnetic flux ropes. *Front. Astron. Space Sci.* **9**, 434. DOI. ADS.

Zhang, X., Guo, J., Guo, Y., Ding, M., Keppens, R.: 2023b, Rotation and Confined Eruption of a Double Flux-Rope System. *arXiv e-prints*, arXiv:2312.07406. DOI. ADS.

Zhao, J., Zhang, P., Gibson, S.E., Fan, Y., Feng, L., Yu, F., Li, H., Gan, W.Q.: 2022, Synthetic Lyman-α emissions for the coronagraph aboard the ASO-S mission. I. An eruptive prominence-cavity system. *Astron. Astrophys.* **665**, A39. DOI. ADS.

Zhong, Z., Guo, Y., Ding, M.D.: 2021, The role of non-axisymmetry of magnetic flux rope in constraining solar eruptions. *Nature Com.* **12**, 2734. DOI. ADS.

Zhou, Z., Cheng, X., Zhang, J., Wang, Y., Wang, D., Liu, L., Zhuang, B., Cui, J.: 2019, Why Do Torus-unstable Solar Filaments Experience Failed Eruptions? *Astrophys. J. Lett.* **877**(2), L28. DOI. ADS.